Applied Surface Science 369 (2016) 58–66

Contents lists available at ScienceDirect

Applied Surface Science

journal homepage: www.elsevier.com/locate/apsusc

The effect of microstructural properties of $CoCr_2O_4$ spinel oxides on catalytic combustion of dichloromethane

Jing-Di Liu, Ting-Ting Zhang, Ai-Pin Jia, Meng-Fei Luo, Ji-Qing Lu *

Key Laboratory of the Ministry of Education for Advanced Catalysis Materials, Institute of Physical Chemistry, Zhejiang Normal University, Jinhua 321004, China

ARTICLE INFO

Article history:
Received 2 January 2016
Received in revised form 1 February 2016
Accepted 5 February 2016
Available online 6 February 2016

Keywords:
Dichloromethane combustion
$CoCr_2O_4$
Microstructure
Reducibility
Surface acidity

ABSTRACT

It was found that a series of spinel $CoCr_2O_4$ oxides were very active and selective for dichloromethane combustion, and the best performance was obtained on a catalyst calcined at 600 °C (with a areal specific reaction rate of 3.41×10^{-8} mol_{CH2Cl2} s^{-1} m^{-2} at 220 °C). Quantitative analyses revealed that Cr^{3+}/Cr^{6+} cations could partially substitute Co^{3+} cations in the octahedral sites of the spinel oxide at high-temperature calcination and thus to enhanced reducibility and surface acidity of the oxide, which synergistically governed the observed catalytic behaviors. Moreover, it was found that high valent Cr species (Cr^{6+}) played very important role in the reaction, with a much higher turnover frequency (2.2×10^{-3} s^{-1}) than that of the Cr^{3+} (0.56×10^{-3} s^{-1}).

© 2016 Elsevier B.V. All rights reserved.

1. Introduction

Chlorinated volatile organic compounds (CVOCs) are generated from various industrial processes such as the manufacture of herbicides, plastics and solvents. Dichloromethane (CH_2Cl_2) is a representative CVOCs, which is harmful to the respiratory system and central nervous system of human [1]. Catalytic combustion is an effective way for the abatement of CVOCs because of its advantages over thermal destruction such as lower operating temperature and higher destructive efficiency [2]. Highly efficient catalyst systems are the core of catalytic combustion of CVOCs, which mainly include supported noble metals (such as Pt and Pd) [3–6], transition metal oxides such as supported Cr-containing materials [7–17] and perovskite-type oxides [18–20], zeolites [21–25].

Cr-containing oxides are very effective for CVOCs oxidation. For example, CrO_x supported on TiO_2 was more active for the oxidation of 1,2-dichlorobenzene compared to other TiO_2-supported oxides (e.g. V_2O_5, MoO_3, Fe_2O_3, and Co_3O_4) [12]. CrO_x supported on active carbon was also active for deep oxidation of CH_2Cl_2 due to the presence of highly dispersed Cr^{6+} species on the catalyst surface [14]. However, the main disadvantages of the Cr-containing catalysts are that they usually deactivate due to the loss of active CrO_x species during the reaction, and the possible formation of toxic chromium oxychloride at low temperature [21], which could limit their potential applications.

Alternatively, structured oxides with Cr species confined in a robust matrix may overcome the disadvantages of the supported Cr catalysts. Therefore, spinel type cobalt chromite oxide ($CoCr_2O_4$) has attracted much attention in catalysis, particularly for CVOCs oxidation. For example, it was reported that the spinel type $CoCr_2O_4$ showed superior performance to other supported Cr catalysts such as CrO_x/Al_2O_3 and CrO_x/MCM-41 in total oxidation of trichloroethylene due to the presence of abundant surface Cr^{3+} species in the $CoCr_2O_4$ oxide [26]. However, quantitative analysis of the effect of microstructures on the physical/chemical properties and consequently catalytic behaviors of the spinel oxides has been rarely investigated, rendering it difficult to obtain a better understanding of this system. Therefore, in this work, detailed characterizations of the microstructures of the $CoCr_2O_4$ spinel oxide was conducted and their significant influences on the observed catalytic behaviors for CH_2Cl_2 combustion has been discussed in a quantitative manner.

2. Experimental

2.1. Catalyst preparation

The $CoCr_2O_4$ catalysts were prepared with a co-precipitation method. 50 mmol of $Co(NO_3)_3{\cdot}6H_2O$ (99.0%) and 50 mmol of $Cr(NO_3)_3{\cdot}9H_2O$ (99.0%) were dissolved in 100 ml distilled water.

* Corresponding author.
E-mail address: jiqinglu@zjnu.cn (J.-Q. Lu).

http://dx.doi.org/10.1016/j.apsusc.2016.02.036
0169-4332/© 2016 Elsevier B.V. All rights reserved.

The mixture was added drop-wise to an aqueous solution containing 200 mmol of NH_4HCO_3 kept at 75 °C. After the precipitation was completed, the suspension was filtered and washed with distilled water and ethanol for 3 times, then the solid was dried at 100 °C overnight. The solid was divided to four parts, followed by calcination in static air at different temperatures (400–700 °C) for 4 h. The obtained catalysts were designated as $CoCr_2O_4$-*x*, with *x* referring to calcination temperature. Also, reference pure Co_3O_4 and Cr_2O_3 oxides were prepared by calcination of $Co(NO_3)_3{\cdot}6H_2O$ and $Cr(NO_3)_3{\cdot}9H_2O$ at 600 °C for 4 h, respectively.

2.2. Characterizations

Surface areas of the catalysts were measured by N_2 adsorption at 77 K on a Quantachrome Autosorb-1 apparatus after pretreatment at 120 °C for 6 h in vacuum. The contents of Co and Cr in the catalysts were determined by X-ray fluorescence (XRF) analysis (ARL ADVANT'X Intelli Power 4200 scanning X-ray fluorescence spectrometer). X-ray diffraction (XRD) patterns were recorded with a PANalytical XíPert PRO MPD powder diffractometer using Cu Kα radiation, operated at 40 kV and 40 mA. Crystallite sizes and lattice parameters of the catalysts were analyzed using a JADE 6.5 software. High resolution transmission electron microscopy (HRTEM) was performed on a JEM-2100F microscopy operated at 200 kV.

Reducibility of the catalyst was measured by hydrogen temperature-programmed reduction (H_2-TPR). 25 mg of the catalyst was placed in a quartz reactor and pretreated in a O_2 flow (20 ml min^{-1}) at 300 °C for 1 h, then it was cooled down to 50 °C. The sample was heated from 50 to 900 °C with a rate of 10 °C min^{-1} under a mixture of 5% H_2–95% N_2 (20 ml min^{-1}). The amount of H_2 consumption was determined by a gas chromatograph with a thermal conductivity detector (TCD), and the H_2 consumption was calibrated by the reduction of a known CuO powder sample.

The surface acidity of the catalyst was measured by ammonia temperature programmed desorption (NH_3-TPD). 50 mg of the catalyst was pretreated in a flow of N_2 at 300 °C for 0.5 h, and then was cooled down to 40 °C. Afterwards, a NH_3 flow (20 ml min^{-1}) was introduced to the sample for 15 min, followed by purging at 80 °C for 0.5 h with a N_2 flow. Then the sample was heated from 40 to 600 °C at a rate of 10 °C min^{-1}, and the profile was recorded using a gas chromatograph with a TCD detector.

The oxidation states of the samples were analyzed by X-ray photoelectron spectra on an ESCALAB 250Xi instrument with a Al Kα X-ray source (1486.6 eV). The binding energy (BE) of C1s core level at 284.8 eV was taken as the internal standard.

Temperature-programmed surface reaction (TPSR) was conducted on a home-made reactor connected with a mass spectrometer (MS, Qic-20 Benchtop, HidenAnalytical). 50 mg of the catalyst was pretreated in a flow of air (20 ml min^{-1}) at 300 °C for 0.5 h, and then was cooled down to 50 °C. A flow of CH_2Cl_2/air mixture (20 ml min^{-1}, 3000 ppm CH_2Cl_2) was introduced to the reactor and the sample was heated from 50 to 400 °C at a rate of 10 °C min^{-1}. And *m*/*e* signals of 70, 44, 18, 36.5, 50.5 and 30 were monitored, corresponding to Cl_2, CO_2, H_2O, HCl, CH_3Cl and HCHO, respectively. Also, the effluent gas was first passed through a $CaCl_2$ filter to remove H_2O, in order to prevent the possible damage of the MS.

The CH_2Cl_2 chemisorption experiments were measured by break-through curves. 50 mg of the catalyst was pretreated in a flow of O_2 (20 ml min^{-1}) at 300 °C for 0.5 h, and then was cooled down to 200 °C. Then a flow of CH_2Cl_2/He mixture (total flow rate = 20 ml min^{-1}, CH_2Cl_2 concentration = 3000 ppm) was introduced to the reactor. Meanwhile, the outlet CH_2Cl_2 signal was monitored by a MS (Qic-20 Benchtop, HidenAnalytical) with a *m*/*e* = 97 (CH_2Cl_2). The amount of chemisorbed CH_2Cl_2 could be calculated based on the profile. Dead volume of the apparatus was also subtracted by running a blank test with the same volume of quartz sand.

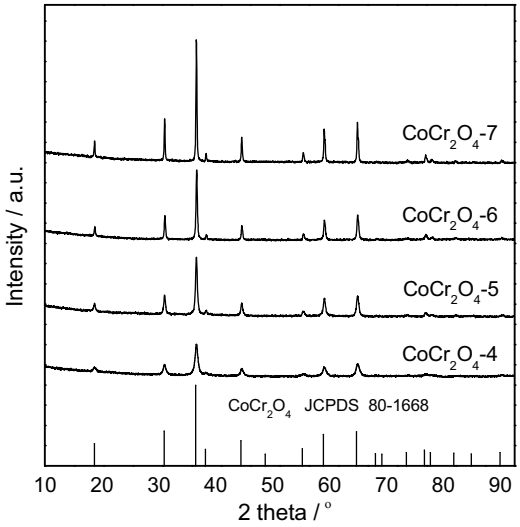

Fig. 1. XRD patterns of various catalysts.

2.3. Activity test

Catalytic test was performed in a fixed-bed reactor (i.d. = 9 mm), loaded with 1.0 g catalyst in 40–60 mesh diluted to 2 ml with quartz sand. The CH_2Cl_2 was introduced to the reactor via passing moisture-containing air through a quartz beaker containing liquid CH_2Cl_2 kept at 0 °C. The reaction conditions were as follows: Concentration of CH_2Cl_2 was 3000 ppm; water vapor concentration was 12,000 ppm; total flow rate was 500 ml min^{-1}; space velocity was 15000 h^{-1}. The conversion of CH_2Cl_2 was analyzed by a gas chromatograph (Shimadzu, GC-14C) equipped with a FID detector. The outlet reaction mixture was neutralized by passing through a 0.1 M NaOH aqueous solution.

Conversion of CH_2Cl_2 was calculated as follows:

$$X_{CH_2Cl_2} = \frac{[CH_2Cl_2]_{in}\text{vol.\%} - [CH_2Cl_2]_{out}\text{vol.\%}}{[CH_2Cl_2]_{in}\text{vol.\%}}$$

where $[CH_2Cl_2]_{in}$ and $[CH_2Cl_2]_{out}$ were the CH_2Cl_2 concentrations in the inlet and outlet gas (vol.%), respectively.

The kinetic study was performed on the same reactor for catalytic test. The CH_2Cl_2 conversion was less than 15% to ensure a differential reaction mode and the reaction conditions were the same as in the catalytic test. Also, the absence of mass transport resistances and hear transfer was guaranteed by evaluation with Weisz-Prater criterion and Mears' criterion, respectively [27].

3. Results

3.1. Catalyst characterizations

Table 1 shows that the surface area of the catalyst gradually declines due to the sintering of crystallites under high temperature. The actual contents of Co and Cr in the catalysts are 24.2 and 40.6 wt.%, respectively, which corresponds to a Co/Cr molar ratio of 0.52.

The XRD patterns of the catalysts (Fig. 1) perfectly match the standard diffractions of spinel $CoCr_2O_4$ (JCPDS 80-1668). No diffractions of CoO_x or CrO_x could be detected, indicating that either the absence of such species or highly dispersed CoO_x or CrO_x in the catalysts. The $CoCr_2O_4$-4 has a crystallite size of 14.8 nm (Table 1), which is much lower than that of the $CoCr_2O_4$-7 (41.3 nm).

Table 1
Physical properties of various catalysts.

Catalyst	S_{BET}/m^2 g^{-1}	Content/wt.%		Cell const./nm	Cryst. size/nm	Surface/bulk ratio[a]
		Co	Cr			
$CoCr_2O_4$-4	53.7	24.2	40.6	0.8311	14.8	0.405
$CoCr_2O_4$-5	27.6	24.2	40.6	0.8315	22.4	0.268
$CoCr_2O_4$-6	17.8	24.2	40.6	0.8324	30.8	0.195
$CoCr_2O_4$-7	10.8	24.2	40.6	0.8332	41.3	0.145
Cr_2O_3	19.9	23.9	40.5	–	–	
Co_3O_4	13.6	–	–	–	–	

[a] The ratio equals 6/D if a close-packed spherical mode is assumed (D is the crystallite size).

Consequently, the surface/bulk ratio (6/D, D refers to crystallite size of the sample) of the catalyst gradually decreases if a close-packed spherical mode is assumed. In addition, the cell parameter gradually increases with calcination temperature, due to disordering of the cations in the spinel structures [28] because of the replacement of Co^{3+} ions (ionic radius of 0.0545 nm) by Cr^{3+} ions (ionic radius of 0.0615 nm).

HRTEM images (Fig. 2) exhibit well crystallized particles in all the catalysts, and the exposed (111) and (220) planes are confirmed by the d-space fringe measurements of 0.506–0.523 and 0.308–0.318 nm, respectively. Interestingly, the fringe values increase with calcination temperature, which is in good agreement with the cell parameters (Table 1).

Fig. 3 and Table 2 show the oxidation states of the elements in the catalysts and their surface compositions. The resolved Co $2p_{3/2}$ spectra (Fig. 3a) contain three components at BEs of 781.1, 782.8 and 787.7 eV, assigning to Co^{2+}, Co^{3+} and satellite peak of Co^{2+} [29,30], respectively. The deconvoluted peak of the Cr $2p_{3/2}$ spectra (Fig. 3b) show three peaks at BEs of 575.6, 576.8 and 578.4, assigning to $Cr(OH)_3$ or Cr_2O_3 [31], Cr^{3+} (occupied octahedral sites) [32] and Cr^{6+} [33], respectively. The presence of Cr^{6+} in spinel $CoCr_2O_4$ oxides was reported in literature and these Cr^{6+} species enriched on the surface [33]. The O 1s spectra (Fig. 3c) could be resolved to two peaks at 530.4 and 531.4 eV, assigning to lattice oxygen (O_{latt}) and adsorbed oxygen (O_{ads}), respectively [34]. The O_{ads} peaks could be assigned to surface chemisorbed oxygen and/or hydroxyl species [35]. The surface contents of Co^{3+}, Cr^{6+} and O_{ads} in these catalysts (Table 2) decline with calcination temperature. The declining surface content of Co^{3+} indicates the transformation of Co^{3+} to Co^{2+}. While the decline in the Cr^{6+} species is probably due to the decomposition of CrO_3 at high temperature (higher than 500 °C) [36], which is accompanied by the change in the content of O_{ads} because the unsaturated Cr^{6+} would adsorb some amount of oxygen in the form of neutral molecules O_2 or bond with electrophilic oxygen O_2^- to keep charge balance [37]. The Cr_{tot}/Co_{tot} ratios (6.50–6.68) in the catalysts is much larger than that of the bulk value (Cr_{bulk}/Co_{bulk} = 2), suggesting the enrichment of Cr species on the surface. Meanwhile this ratio gradually increases with calcination temperature, indicating changes in the distribution of Co and Cr species on the surface. The densities of the surface species could be further calculated based on the surface compositions, surface areas and surface bulk ratios. The densities of surface Co^{3+} species in the catalysts (12.4–17.4 μmol m^{-2}) are much lower than those of the Cr species (66.4–118.3 μmol m^{-2}). Furthermore, the Cr^{3+} density increases with calcination temperature while that of the Cr^{6+} reaches a maximum at 600 °C (25.1 μmol m^{-2}).

Fig. 4(a) shows the H_2-TPR profiles of the catalysts. The weak peak centered at 350 °C (α) is due to the reduction of Cr^{6+} to Cr^{3+} [38] and/or that of Co^{3+} to Co^{2+} [39]. The intense peak at 500–700 °C (β) is due to the reduction of Cr^{3+} to lower oxidation states [40] and Co^{2+} to Co^0 [39]. The H_2 consumptions of the α peak are 0.322, 0.214, 0.250 and 0.117 mmol g_{cat}^{-1} for the $CoCr_2O_4$-4, $CoCr_2O_4$-5, $CoCr_2O_4$-6 and $CoCr_2O_4$-7, respectively. Then, the overall molar contents of high valent Cr and Co species ($Cr^{6+} + Co^{3+}$) in the $CoCr_2O_4$-4, $CoCr_2O_4$-5, $CoCr_2O_4$-6 and $CoCr_2O_4$-7 are 1.21, 0.81, 0.95 and 0.44 mol.%, respectively. These values suggest that the dominant Cr and Co species in the catalysts are Cr^{3+} and Co^{2+}, which matches the nominal formula of $CoCr_2O_4$. Note that the Cr^{6+} and Co^{3+} surface contents are much higher (XPS, Table 2), suggesting that these high-valent species are mainly located on the surface. Moreover, the normalized H_2 consumptions based on surface areas (Fig. 4b) indicates that the $CoCr_2O_4$-6 has the highest value (14.0 μmol m^{-2}) compared to the other samples, implying the best reducibility of this catalyst.

NH_3-TPD profiles (Fig. 5a) demonstrate that all the samples show a weak desorption peak at about 150 °C (α) and two overlapped intense peaks in 250–500 °C (β and γ), suggesting the presence of surface acidic sites with various properties. The amounts of NH_3 desorption are 0.19, 0.26, 0.27 and 0.14 mmol g_{cat}^{-1} for the $CoCr_2O_4$-4, $CoCr_2O_4$-5, $CoCr_2O_4$-6 and $CoCr_2O_4$-7, respectively. Such volcano trend of the surface acidity clearly suggests that calcination temperature remarkably influences the surface acidity of the cobalt chromites [41], which is related to the microstructures of the samples. Also, the normalized surface acidity in Fig. 5b shows that the $CoCr_2O_4$-6 has the highest value (15.2 μmol m^{-2}).

3.2. Catalytic performance

Fig. 6a shows that the overall activity follows an order of $CoCr_2O_4$-6 > $CoCr_2O_4$-5 > $CoCr_2O_4$-7 > $CoCr_2O_4$-4 > Cr_2O_3 > Co_3O_4, with T_{50} (the temperature at which a conversion of 50% is obtained) values of 210, 242, 258, 264, 292 and 351 °C, respectively. The higher activity of the spinel catalysts than the Cr_2O_3 suggests the advantage of the spinel structure. Besides, it seems that the Cr species in the spinel are more active than the Co species in spinel since Co_3O_4 also has a spinel structure [42] but it is much less active than the $CoCr_2O_4$. The spinel catalysts outperform other Cr-containing systems such as CrO_3/C [0.022×10^{-3} $mmol_{CH2Cl2}$ g_{cat}^{-1} h^{-1} at 250 °C], [43], Pd/CrZr [0.642×10^{-3} $mmol_{CH2Cl2}$ g_{cat}^{-1} h^{-1} at 250 °C], [44] and CrAlO [0.241 $mmol_{CH2Cl2}$ g_{cat}^{-1} h^{-1} at 250 °C], [45]. Also, the reaction rate on the $CoCr_2O_4$-6 catalyst at 250 °C is 2.96 $mmol_{CH2Cl2}$ g_{cat}^{-1} h^{-1}, which is 12-fold as high as that obtained on a K-promoted Pt/Al_2O_3 catalyst (1.085 $mmol_{CH2Cl2}$ g_{cat}^{-1} h^{-1}) reported in our previous work [6]. Also, areal specific reaction rates of the catalysts at 220 °C (Fig. 6b) reveal that the $CoCr_2O_4$-6 and $CoCr_2O_4$-7 are much more active than the $CoCr_2O_4$-4 and $CoCr_2O_4$-5, which is up to 7-fold. The Arrhenius plots and the apparent activation energies (Fig. 7) follow an order of $CoCr_2O_4$-6 (99.3 kJ mol^{-1}) < $CoCr_2O_4$-5 (102.9 kJ mol^{-1}) < $CoCr_2O_4$-7 (113.1 kJ mol^{-1}) < $CoCr_2O_4$-4 (117.5 kJ mol^{-1}), which is in line with the observed order of reactivity (Fig. 6).

The final products on the spinel catalysts are CO_2, Cl_2, HCl and H_2O, without by-products such as HCHO and CH_3Cl (Fig. 8a), indicating that these catalysts are very selective due to the abundance of its Cr^{3+} species [26]. The surface reaction of $CH_2Cl_2 + O_2$ over $CoCr_2O_4$ spinel oxide went through a formate intermediate, which

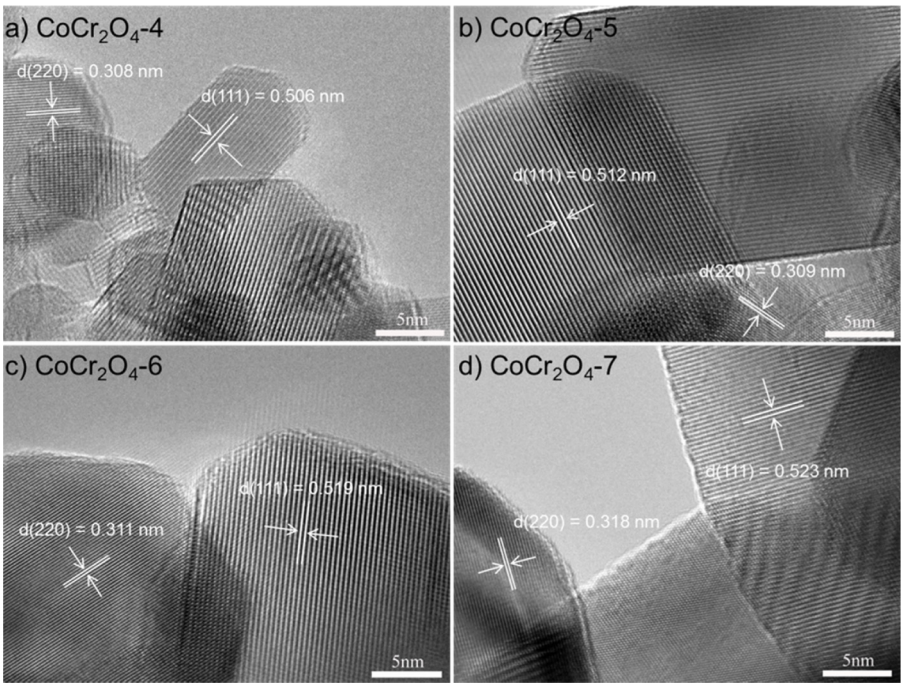

Fig. 2. HRTEM images of various catalysts.

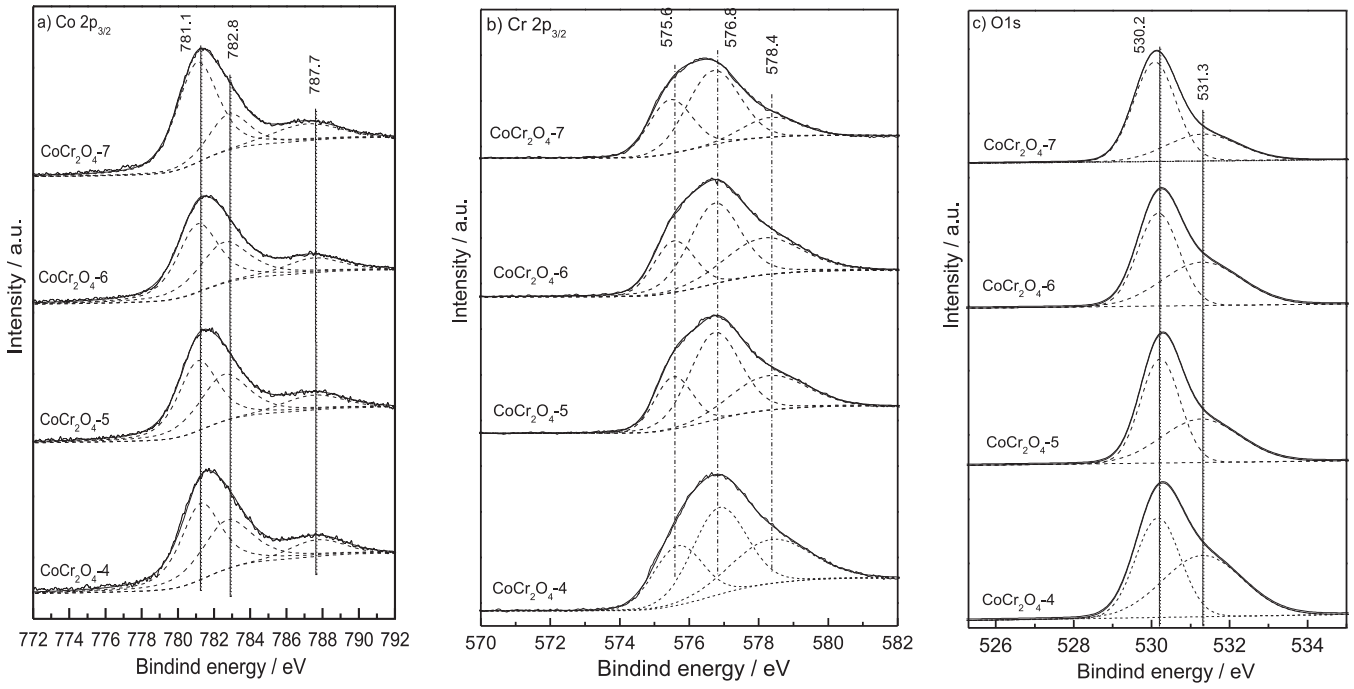

Fig. 3. XPS spectra of (a) Co 2p 3/2, (b) Cr 2p 3/2 and (c) O 1s of various catalysts.

Table 2
Surface composition analyses of various catalysts.

Catalyst	Surface atomic ratio				Density of surface species/μmol m^{-2}			
	Co^{3+}/Co_{tot} [a]	Cr^{6+}/Cr_{tot} [b]	O_{ads}/O_{tot}	Cr_{tot}/Co_{tot}	Co^{3+}	Total Cr	Cr^{3+}	Cr^{6+}
$CoCr_2O_4$-4	0.39	0.28	0.36	6.50	12.9	66.4	47.8	18.6
$CoCr_2O_4$-5	0.38	0.26	0.35	6.55	16.3	85.6	63.3	22.3
$CoCr_2O_4$-6	0.36	0.26	0.32	6.62	17.4	96.5	71.4	25.1
$CoCr_2O_4$-7	0.21	0.14	0.22	7.10	12.4	118.3	101.7	16.6

[a] $Co^{3+}/Co_{tot} = Co^{3+}/(Co^{3+} + Co^{2+})$.
[b] $Cr^{6+}/Cr_{tot} = Cr^{6+}/(Cr^{3+} + Cr^{6+})$.

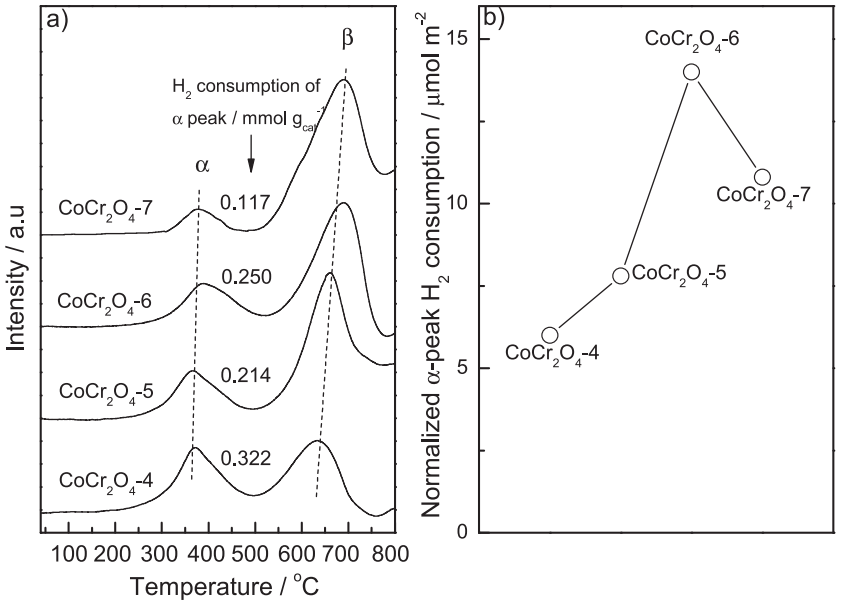

Fig. 4. (a) H_2-TPR profiles and (b) normalized α-peak H_2 consumption of various catalysts.

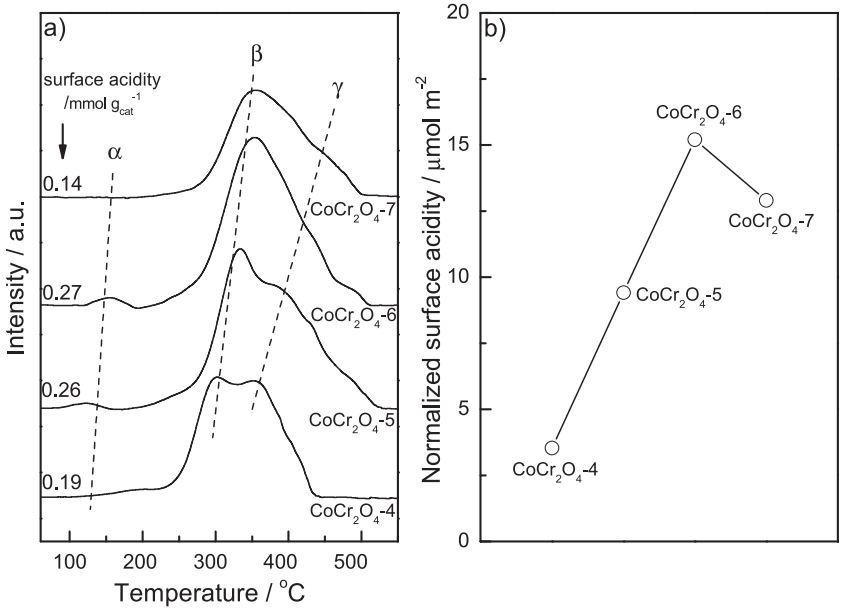

Fig. 5. (a) NH_3-TPD profiles and (b) normalized surface acidity of various catalysts.

could be decomposed to CO and further oxidized to CO_2 [46]. Also, the catalysts are quite stable during the 10 h reaction, which implies that there is no catalyst deactivation (Fig. 8b).

4. Discussion

The areal specific reaction rates (Fig. 6b) further indicate that the catalysts calcined at high temperatures (e.g. 600 or 700 °C) are more active than those calcined at low temperatures (e.g. 400 or 500 °C). Such finding clearly implies that the microstructure of the catalyst may significantly alter upon calcination and thus deserves a discussion.

In case of $CoCr_2O_4$ spinel oxide, the Cr cations will only locate at the octahedral sites, while the Co^{2+} and Co^{3+} will locate at tetrahedral and octahedral sites, respectively [47] and the occupied octahedral sites are exposed at the surface and regarded as active sites for the oxidation reaction [32]. Thus, the formula could be expressed as $Co^{2+}[Co^{3+}_{2-x}Cr^{3+}_{x}]O_4$. Besides, Cr^{6+} species were detected in the catalyst (Fig. 3b, Table 2 and Fig. 4), thus the formula could be modified to $Co^{2+}[Co^{3+}_{2-x}Cr^{3+}_{y}Cr^{6+}_{(x-y)/2}\square_{(x-y)/2}]O_4$ (□ refers to vacancy) [47]. Such octahedral coordinated Cr^{6+} ions would give rise to a local distortion of spinel lattice according to Jahn–Teller effect [48]. A simple model of the $CoCr_2O_4$ spinel oxide is demonstrated in Fig. 9. For the low-temperature calciend oxide (e.g. $CoCr_2O_4$-4), the octahedral sites are dominantly occupied by Cr cations (Cr^{3+} and Cr^{6+}) but some are occupied by Co^{3+} cations (indicated by dash circles). For the high-temperature calcined oxide (e.g. $CoCr_2O_4$-7), some Cr^{3+} ions could re-occupy the octahedral sites by replacing the Co^{3+} cations, which is justified by the increasing lattice parameters of the $CoCr_2O_4$ oxides (Table 1) and the increasing surface Cr_{tot}/Co_{tot} ratio upon calcination temperature (Table 2), as well as the increasing lattice fringes (Fig. 2).

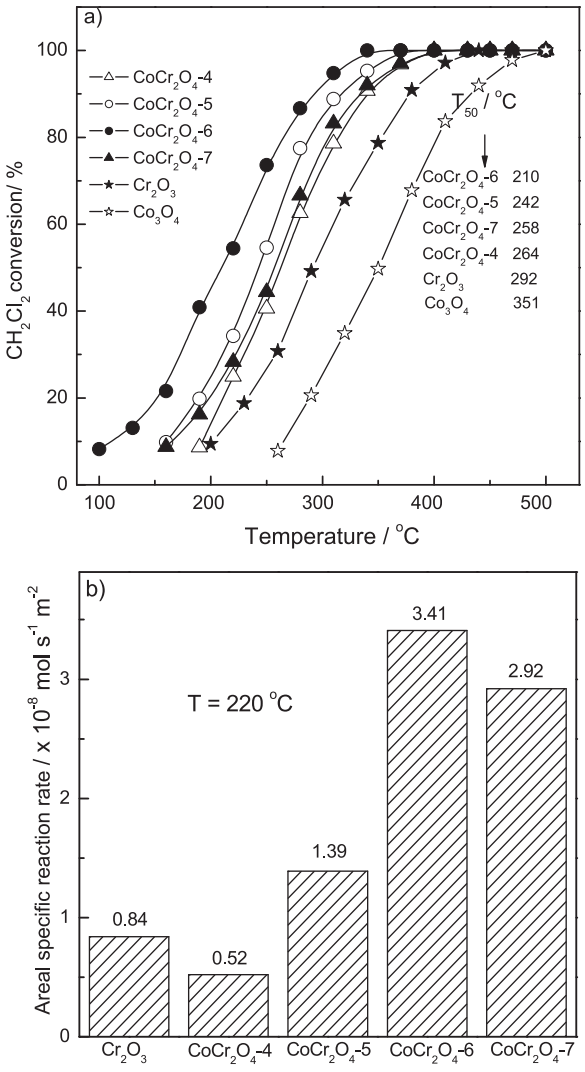

Fig. 6. (a) Light-off curves and (b) areal specific reaction rates of various catalysts.

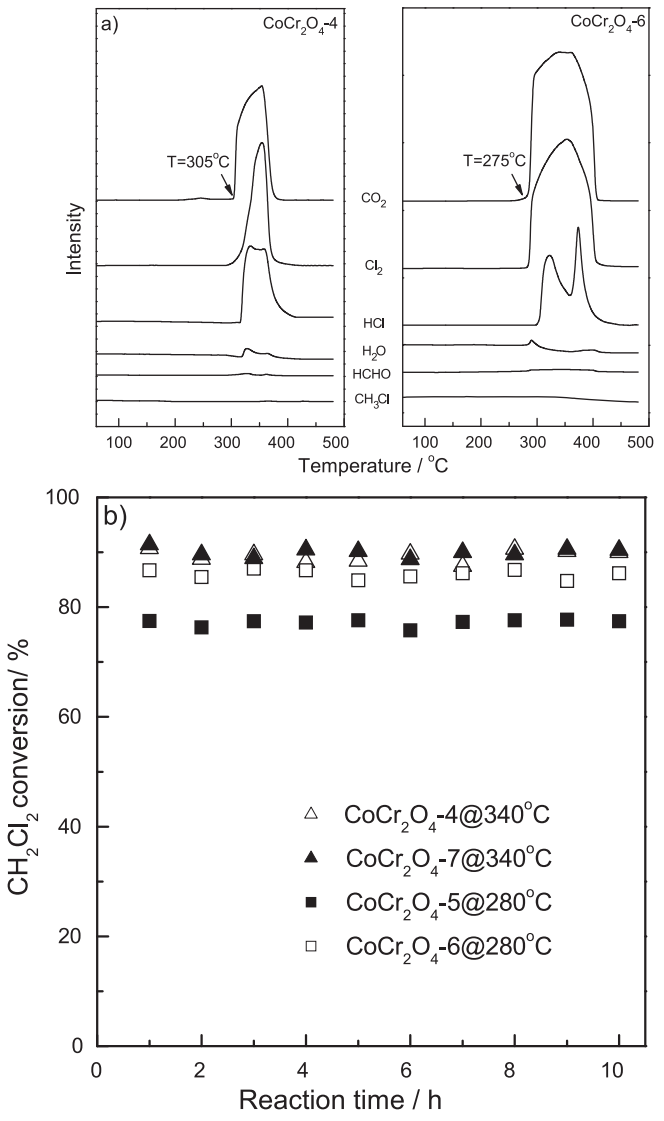

Fig. 8. (a) Product distributions on $CoCr_2O_4$-4 and $CoCr_2O_4$-6; (b) stability of various catalysts.

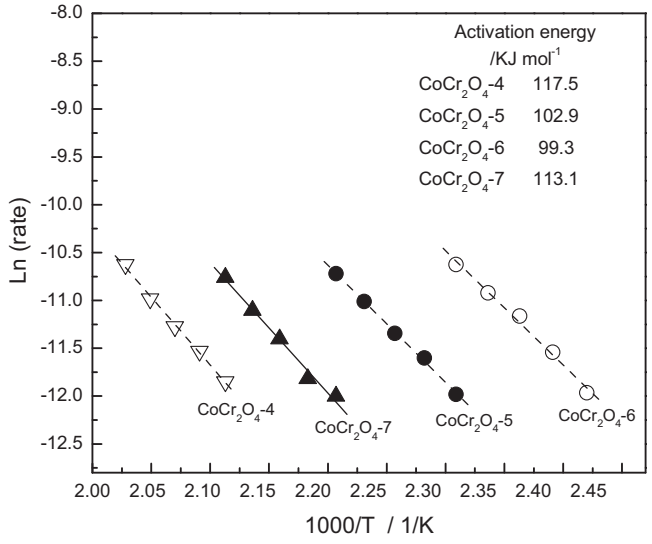

Fig. 7. Arrhenius plots of CH_2Cl_2 oxidation over various catalysts.

The consequences of the microstructural changes of the catalysts are the variations of their physical/chemical properties, which are related to the changes of the oxidation states of the Co and Cr species. First of all, the normalized low-temperature H_2 consumption values for the catalysts (Fig. 4b) follow the same order of the surface densities of the Co^{3+} and Cr^{6+} species (Table 2), suggesting the participation of these species during the reduction process in low temperature region. Secondly, the surface acidity is also related to the exposed octahedral sites in the spinel oxide [32], which is strongly dependent on the polarity of the metal cations [49]. When the $CoCr_2O_4$ oxide was calcined at elevated temperature, Co^{3+} cations at octahedral sites were gradually substituted by Cr^{3+} or Cr^{6+} cations, which leads to enhanced surface acidity because Cr^{3+} or Cr^{6+} cations are more polarized than the Co^{3+} cations, which is in line with the finding by Wang et al. [50]. Therefore, the high temperature calcination of the spinel $CoCr_2O_4$ oxide results in the partial substitution of Cr species (Cr^{3+} or Cr^{6+}), which consequently leads to the enhanced low-temperature catalyst reducibility and surface acidity compared to that calcined at low temperature, which are correlated to the densities of exposed Co^{3+}, Cr^{3+}/Cr^{6+} species.

For the CVOCs oxidation, the catalytic behavior is governed by catalyst reducibility and surface acidity. The catalyst reducibility

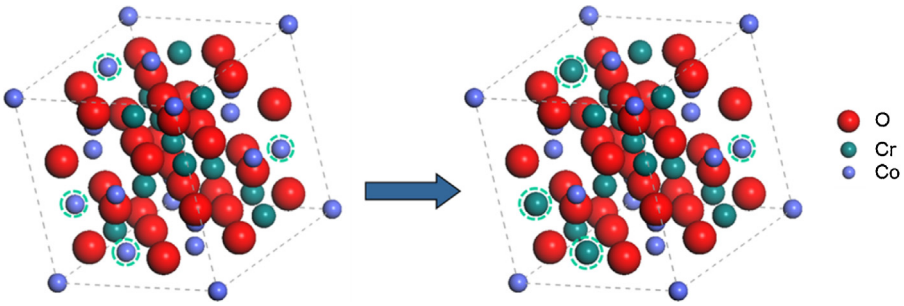

Fig. 9. Microstructural change of $CoCr_2O_4$ at low and high temperature calcination.

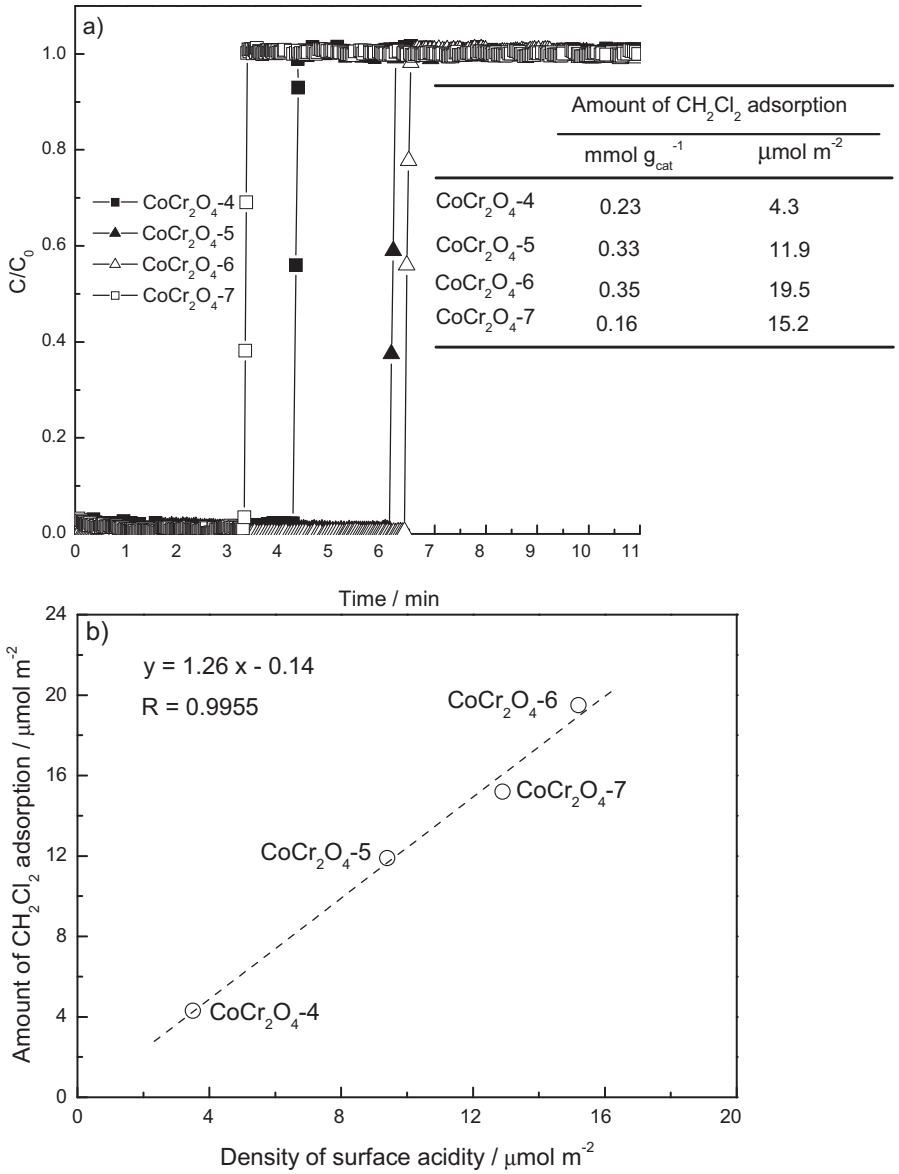

	Amount of CH_2Cl_2 adsorption	
	mmol g_{cat}^{-1}	μmol m^{-2}
$CoCr_2O_4$-4	0.23	4.3
$CoCr_2O_4$-5	0.33	11.9
$CoCr_2O_4$-6	0.35	19.5
$CoCr_2O_4$-7	0.16	15.2

Fig. 10. (a) Break-through curves of CH_2Cl_2 adsorption on various catalysts; (b) Correlation between density of surface acidity and amount of adsorbed CH_2Cl_2.

correlates to the mobility and the activation of the oxygen species [51], and the surface acid sites are effective for the adsorption of CH_2Cl_2 and the rupture of the C—Cl bond of chloroalkanes [52]. The adsorption of CH_2Cl_2 on the catalyst surface was verified by the break-through curves (Fig. 10a). The normalized amounts of adsorbed CH_2Cl_2 on the $CoCr_2O_4$-4, $CoCr_2O_4$-5, $CoCr_2O_4$-6 and $CoCr_2O_4$-7 are 4.3, 11.9, 19.5 and 15.2 $\mu mol\,m^{-2}$, respectively, which fit linearly with the density of surface acidity, as shown in Fig. 10b. Such plot confirms that the surface acidic sites are the centers for the CH_2Cl_2 adsorption, and thus play very important role in the reaction. However, the slope is slightly larger than unity, implying physisorption of CH_2Cl_2 on the surface must occur.

The areal specific reaction rates of the catalysts at 220 °C were plotted as functions of normalized CH_2Cl_2 adsorption and the low

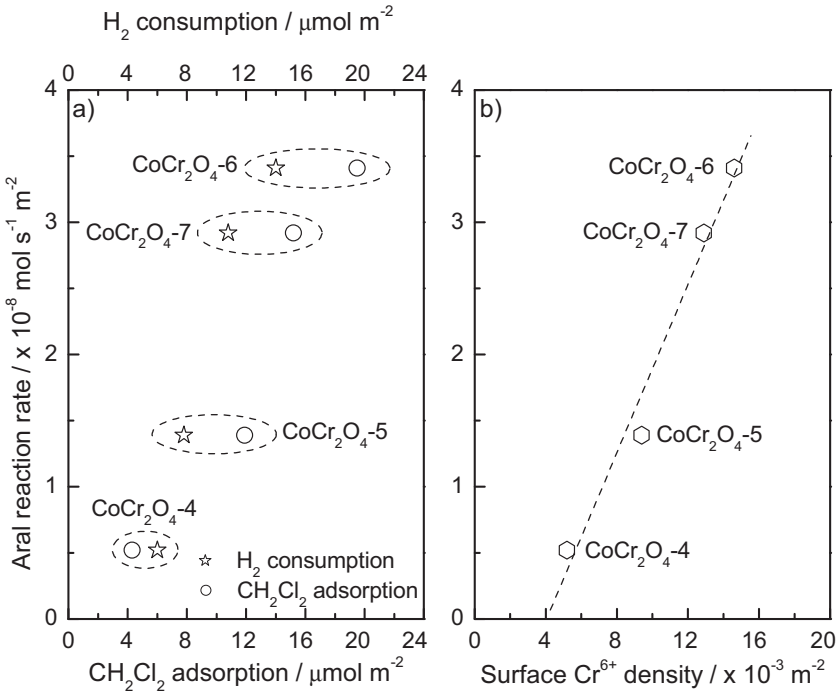

Fig. 11. Correlation between (a) normalized surface acidity, catalyst reducibility and (b) surface Cr^{6+} density and areal reaction rate of $CoCr_2O_4$ catalysts.

temperature H_2 consumption values, as shown in Fig. 11a. It is found that the rate increases with both parameters, which clearly suggests that the catalytic performance is synergistically controlled by catalyst reducibility and surface acidity. This conclusion is in line with the findings on other catalyst systems such as CeO_2-USY [25], $Pt/CeO_2–Al_2O_3$ [51] for CVOCs oxidation. Moreover, Fig. 11b shows the reaction rate is proportional to the Cr^{6+} density, implying the important role of such high valent species. Our finding is consistent with that reported by Kang and Lee [14], in which the authors concluded that highly dispersed Cr^{6+} species on the CrO_x/C were very important for deep oxidation of CH_2Cl_2. In contrast, Kim and Ihm [26] concluded that Cr^{6+} species in the $CoCr_2O_4$ spinel oxide were inactive for the oxidation of trichloroethylene. To clarify the contributions of different Cr species in the reaction, calculation of the turnover frequencies (TOFs) of different Cr species is conducted. Since the reaction occurs at the catalyst surface and the exposed cations in the $COCr_2O_4$ spinel are Co^{3+}, Cr^{3+} and Cr^{6+} at octahedral sites, the specific reaction rate could be expressed as follows:

$$r = D_{Co^{3+}} * \mathrm{TOF}_{Co^{3+}} + D_{Cr^{3+}} * \mathrm{TOF}_{Cr^{3+}} + D_{Cr^{6+}} * \mathrm{TOF}_{Cr^{6+}} \quad (1)$$

where r is areal specific reaction rate, $D_{Co^{3+}}$, $D_{Cr^{3+}}$ and $D_{Cr^{6+}}$ are the densities of surface Co^{3+}, Cr^{3+} and Cr^{6+} species, respectively. $\mathrm{TOF}_{Co^{3+}}$, $\mathrm{TOF}_{Cr^{3+}}$ and $\mathrm{TOF}_{Cr^{6+}}$ are TOFs of the Co^{3+}, Cr^{3+} and Cr^{6+} species, respectively. Note that the contribution of the Co^{3+} species is very limited as the Co_3O_4 is not active at low temperature (Fig. 6), the expression could be simplified to

$$r = D_{Cr^{3+}} * \mathrm{TOF}_{Cr^{3+}} + D_{Cr^{6+}} * \mathrm{TOF}_{Cr^{6+}} \quad (2)$$

By using the data in Fig. 6b and Table 2 and doing a multi-linear regression, the TOFs of Cr^{3+} and Cr^{6+} at 220 °C are 0.56×10^{-3} and 2.2×10^{-3} s^{-1}, respectively, which clearly suggest the higher activity of Cr^{6+} species than that of Cr^{3+} in the spinel oxide. The higher activities of the Cr^{6+} cations in the reaction are probably due to the enhanced reducibility or oxidizability compared to those of the Cr^{3+} cations [14] (as evidenced by the H_2-TPR results, Fig. 4b) as well as the enhanced surface acidity (as evidenced by the NH_3-TPD results, Fig. 5b), which are two decisive factors that synergistically govern the reactivity for CVOCs oxidation.

Finally, concerning the reaction mechanism of CH_2Cl_2 oxidation over $CoCr_2O_4$ spinel oxide, it has been reported [46] that the reaction pathways mainly consist of the formation of HCHO (through sequential dehydrochlorination on surface acidic sites) and decomposition of HCHO to CO and CO_2 (through oxidation with O_2 molecules), as evidenced by in situ FTIR results. This mechanism again highlights the important role of surface acidity and reducibility of the catalyst in the reaction.

5. Conclusions

This work demonstrates that $CoCr_2O_4$ spinel oxides are highly active for CH_2Cl_2 oxidation and they are more stable than other Cr-containing system, which provides its promising potential in practical application. The effect of calcination temperature on the microstructures the catalysts and consequently their chemical/physical properties has been quantitatively investigated in detail. The high calcination temperature results in the high exposure of Cr species on the surface and thus enhanced surface acidity and reducibility, which are two main reasons for the improved catalytic performance observed on the catalysts. Moreover, high valent Cr^{6+} species are more active than the Cr^{3+} species.

Acknowledgments

This work is financially supported by Natural Science Foundation of China (Grant No. 21173195).

References

[1] V.H. Vu, J. Belkouch, A. Ould-Dris, B. Taouk, J. Hazard. Mater. 169 (2009) 758–765.
[2] J.R. González-Velasco, A. Aranzabal, J.I. Gutiérrez-Ortiz, R. López-Fonseca, M.A. Gutiérrez-Oritiz, Appl. Catal. B: Environ. 19 (1998) 189–197.
[3] L.F. Wang, M. Sakurai, H. Kameyama, J. Hazard. Mater. 154 (2008) 390–395.

[4] S. Pitkäaho, L. Matejova, S. Ojala, J. Gaalova, R.L. Keiski, Appl. Catal. B: Environ. 113 (2012) 150–159.
[5] A. Musialik-Piotrowska, Catal. Today 119 (2007) 301–304.
[6] Y. Wang, H.H. Liu, S.Y. Wang, M.F. Luo, J.Q. Lu, J. Catal. 311 (2014) 314–324.
[7] B. Chen, C. Bai, R. Cook, J. Wright, C. Wang, Catal. Today 30 (1996) 15–20.
[8] F. Bertinchamps, C. Grégoire, E.M. Gaigneaux, Appl. Catal. B: Environ. 66 (2006) 1–9.
[9] A.M. Padilla, J. Corella, J.M. Toledo, Appl. Catal. B: Environ. 22 (1999) 107–121.
[10] T. Tanilimiş, S. Atalay, H.E. Alpay, F.S. Atalay, J. Hazard. Mater. 90 (2002) 157–167.
[11] H. Rotter, M.V. Landau, M. Herskowitz, Environ. Sci. Technol. 39 (2005) 6845–6850.
[12] S. Krishnamoorthy, J.A. Rivas, M.D. Amiridis, J. Catal. 193 (2000) 264–272.
[13] S.D. Yim, I.-S. Nam, J. Catal. 221 (2004) 601–611.
[14] M. Kang, C.H. Lee, Appl. Catal. A 266 (2004) 163–172.
[15] G.A. Atwood, H.L. Greene, P. Chintawar, R. Rahcapudi, B. Ramachandran, C.A. Vogel, Appl. Catal. B: Environ. 18 (1998) 51–61.
[16] S. Kawi, M. Te, Catal. Today 44 (1998) 101–109.
[17] Q. Huang, Z. Meng, R. Zhou, Appl. Catal. B: Environ. 115–116 (2012) 179–189.
[18] S.X. Chen, Y. Wang, A.P. Jia, H.H. Liu, M.F. Luo, J.Q. Lu, Appl. Surf. Sci. 307 (2014) 178–188.
[19] C. Zhang, W. Hua, C. Wang, Y. Guo, Y. Guo, G. Lu, A. Baylet, A. Giroir-Fendler, Appl. Catal. B: Environ. 134–135 (2013) 310–315.
[20] C. Zhang, C. Wang, W. Zhan, Y. Guo, Y. Guo, G. Lu, A. Baylet, A. Giroir-Fendler, Appl. Catal. B: Environ. 129 (2013) 509–516.
[21] R. Rachapudi, P.S. Chintawar, H.L. Greene, J. Catal. 185 (1999) 58–72.
[22] L. Pinard, J. Mijoin, P. Magnoux, M. Guisnet, J. Catal. 215 (2003) 234–244.
[23] A. Aranzabala, J.A. González-Marcosa, M. Romero-Sáez, J.R. González-Velasco, M. Guillemot, P. Magnoux, Appl. Catal. B: Environ. 88 (2009) 533–541.
[24] J.R. González-Velasco, R. López-Fonseca, A. Aranzabal, J.I. Gutiérrez-Ortiz, P. Steltenpohl, Appl. Catal. B: Environ. 24 (2000) 233–322.
[25] Q. Huang, X. Xue, R. Zhou, J. Hazard. Mater. 183 (2010) 694–700.
[26] D.C. Kim, S.K. Ihm, Environ. Sci. Technol. 35 (2001) 222–226.
[27] H.S. Fogler, Elements of Chemical Reaction Engineering, 4th Ed., Pearson Education Inc., 2006, pp. 839.
[28] G.L. Castiglioni, G. Minelli, P. Porta, A. Vaccari, J. Solid State Chem. 152 (2000) 526–532.
[29] G.C. Allen, S.J. Harris, L.A. Jutson, Appl. Surf. Sci. 37 (1989) 111–134.
[30] W. Wei, W. Chen, D.G. Ivey, Chem. Mater. 20 (2008) 1941–1947.
[31] Y. Lin, W. Cai, X. Tian, X. Liu, G. Wang, C. Liang, J. Mater. Chem. 21 (2011) 991–997.
[32] J.P. Jacobs, A. Maltha, J.R.H. Reintjes, T. Drimal, V. Ponec, H.H. Brongersma, J. Catal. 147 (1994) 294–300.
[33] J. Sloczynski, J. Janas, T. Machej, J. Rynkowski, J. Stoch, Appl. Catal. B: Environ. 24 (2000) 45–60.
[34] K. Rida, A. Benabbas, F. Bouremmad, M.A. Pena, A. Martinez-Arias, Appl. Catal. A: Gen. 375 (2010) 101–106.
[35] A. La Rosa-Toro, R. Berenguer, C. Quijada, F. Montilla, E. Morallon, J.L. Vazquez, J. Phys. Chem. B 110 (2006) 24021–24029.
[36] W.K. Jóźwiak, W. Ignaczak, D. Dominiak, T.P. Maniecki, Appl. Catal. A: Gen. 258 (2004) 33–45.
[37] J. Li, X. Liang, S. Xu, J. Hao, Appl. Catal. B: Environ. 90 (2009) 307–312.
[38] J. Chen, W. Shi, X. Zhang, Environ. Sci. Technol. 45 (2011) 8491–8947.
[39] Y. Xia, H. Dai, H. Jiang, L. Zhang, Catal. Commun. 11 (2010) 1171–1175.
[40] J. Chen, Y. Zhang, H. Arandiyan, Catal. Today 201 (2013) 12–18.
[41] Y. Wang, Z. Zhou, M. Jia, X. Zhu, Catal. Lett. 104 (2005) 67–71.
[42] Y. Wang, C.M. Yang, W. Schmidt, B. Spliethoff, E. Bill, F. Schüth, Adv. Mater. 17 (2005) 53–56.
[43] S.C. Petrosius, R.S. Drago, V. Young, G.C. Grunewald, J. Am. Chem. Soc. 115 (1993) 6131–6137.
[44] L. Jin, R. Ma, J. Lin, L. Meng, Y. Wang, M. Luo, Ind. Eng. Chem. Res. 50 (2011) 10878–10882.
[45] R. Ma, P. Hu, L. Jin, Y. Wang, J. Lu, M. Luo, Catal. Today 175 (2011) 598–602.
[46] Y. Wang, A.P. Jia, M.F. Luo, J.Q. Lu, Appl. Catal. B: Environ. 165 (2015) 477–486.
[47] P. Bracconi, L.C. Dufour, J. Phys. Chem. 79 (1975) 2400–2405.
[48] F.A. Kroger, The Chemistry of Imperfect Crystals, 1st ed., North-Holland Pub. Co., Amsterdam, 1964.
[49] K. Sreekumar, S. Sugunan, Appl. Catal. A: Gen. 230 (2002) 245–251.
[50] Y. Wang, Z. Zhou, M. Jia, X. Zhu, W. Zhang, D. Jiang, Catal. Lett. 104 (2005) 67–71.
[51] Q.Y. Chen, N. Li, M.F. Luo, J.Q. Lu, Appl. Catal. B: Environ. 127 (2012) 159–166.
[52] L. Intriago, E. Díaz, S. Ordó˜nez, A. Vega, Microporous Mesoporous Mater. 91 (2006) 161–169.